





In the format provided by the authors and unedited.

Concurrence of quantum anomalous Hall and topological Hall effects in magnetic topological insulator sandwich heterostructures

Jue Jiang^{1,4}, Di Xiao ^{1,4}, Fei Wang¹, Jae-Ho Shin¹, Domenico Andreoli², Jianxiao Zhang¹, Run Xiao¹, Yi-Fan Zhao¹, Morteza Kayyalha¹, Ling Zhang¹, Ke Wang³, Jiadong Zang², Chaoxing Liu¹, Nitin Samarth ^{1*}, Moses H. W. Chan ^{1*} and Cui-Zu Chang ^{1*}

¹Department of Physics, The Pennsylvania State University, University Park, PA, USA. ²Department of Physics, University of New Hampshire, Durham, NH, USA. ³Materials Research Institute, The Pennsylvania State University, University Park, PA, USA. ⁴These authors contributed equally: Jue Jiang, Di Xiao.
*e-mail: nxs16@psu.edu; mhc2@psu.edu; cxc955@psu.edu

Supplementary Information

Concurrence of Quantum Anomalous Hall and Topological Hall Effects in Magnetic Topological Insulator Sandwich Heterostructures

Jue Jiang^{1,4}, Di Xiao^{1,4}, Fei Wang¹, Jae-Ho Shin¹, Domenico Andreoli², Jianxiao Zhang¹, Run
Xiao¹, Yi-Fan Zhao¹, Morteza Kayyalha¹, Ling Zhang¹, Ke Wang³, Jiadong Zang², Chaoxing
Liu¹, Nitin Samarth¹, Moses H. W. Chan¹, and Cui-Zu Chang¹

¹Department of Physics, The Pennsylvania State University, University Park, PA 16802

²Department of Physics, University of New Hampshire, Durham, NH 03824

³Materials Research Institute, The Pennsylvania State University, University Park, PA 16802

⁴These authors contributed equally to this work.

Corresponding authors: nxs16@psu.edu (N.S.); mhc2@psu.edu (M.H.W.C.); cxc955@psu.edu
(C.Z.C.)

Contents:

- I. Characterizations of the TI sandwich heterostructure**
- II. Determining the Curie temperature of the TI sandwich heterostructure**
- III. Additional transport results of the TI sandwich heterostructure (3-5-3 sample 1)**
- IV. Transport results of the second 3-5-3 TI sandwich heterostructure (3-5-3 sample 2)**
- V. Transport results of TI sandwich heterostructures with different sample configurations**
- VI. Theoretical calculations for the spin susceptibility in magnetic TI**
- VII. Simulation of the quantum transport through a single chiral magnetic domain wall in magnetic TI**

I. Characterizations of the TI sandwich heterostructure

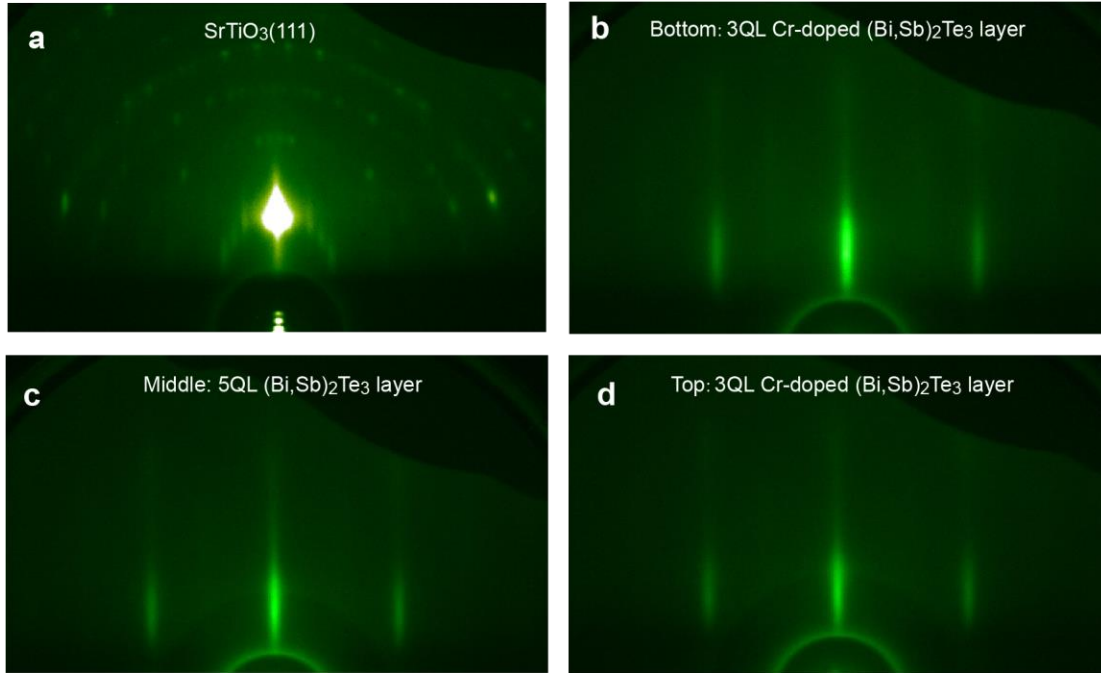


Figure S1 | RHEED patterns of the magnetic TI sandwich heterostructure (3-5-3 sample). (a-d) RHEED patterns of the heat-treated SrTiO₃ (111) substrate (a), the bottom layer of 3QL Cr-doped (Bi, Sb)₂Te₃ (b), the middle layer of 5QL undoped (Bi, Sb)₂Te₃ (c), and the top layer of 3QL Cr-doped (Bi, Sb)₂Te₃ (d).

Figure S1a shows the reflection high-energy electron diffraction (RHEED) patterns of the heat-treated insulating SrTiO₃ (111) substrate, the clear reconstruction indicates an atomically flat surface, which is crucial for growing the high-quality topological insulator (TI) film. **Figures S1b to S1d** show the RHEED patterns of the bottom 3 quintuple layer (QL) Cr-doped (Bi, Sb)₂Te₃ layer, the undoped 5QL (Bi, Sb)₂Te₃ middle layer and the top 3QL Cr-doped (Bi, Sb)₂Te₃ layer, respectively. The sharp and streaky “1×1” patterns observed in each stage indicate the high-quality of our magnetic TI sandwich samples.

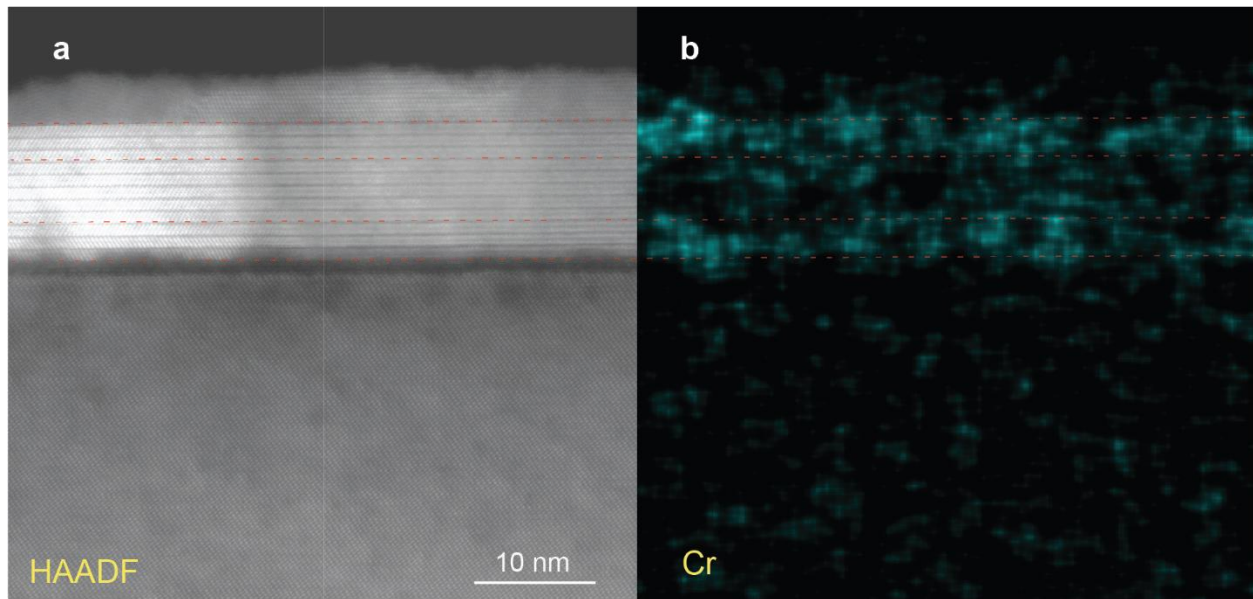


Figure S2 | TEM image and EDS mapping of the magnetic TI sandwich heterostructure (3-5-3 sample). (a) The TEM image of a 3QL Cr-doped $(\text{Bi, Sb})_2\text{Te}_3$ /5QL $(\text{Bi, Sb})_2\text{Te}_3$ /3QL Cr-doped $(\text{Bi, Sb})_2\text{Te}_3$ sandwich heterostructure. The total thickness is 11QL. (b) EDS map of the Cr ions of the 3-5-3 sample.

Figure S2a shows a cross-sectional transmission electron microscope (TEM) image of a 3QL Cr-doped $(\text{Bi, Sb})_2\text{Te}_3$ /5QL $(\text{Bi, Sb})_2\text{Te}_3$ /3QL Cr-doped $(\text{Bi, Sb})_2\text{Te}_3$ sandwich heterostructure (3-5-3 sample). The crystal structures of Te capping layer, the 11QL heterostructure, and the SrTiO_3 substrate can be clearly distinguished. The corresponding energy-dispersive X-ray spectroscopy (EDS) mapping of Cr (**Fig. S2b**) shows that Cr signal is stronger in the top and the bottom 3QL TI layers, consistent with the diluted Cr doping ($\sim 7.5\%$) in these two layers.

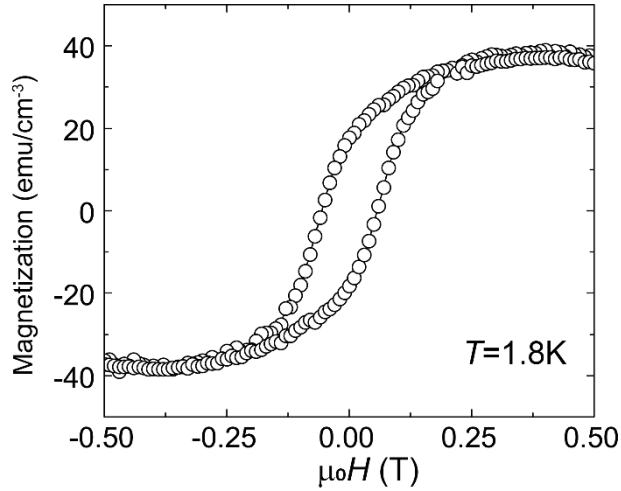


Figure S3 | Magnetic hysteresis loop of the magnetic TI sandwich heterostructure (3-5-3 sample) measured by SQUID at $T = 1.8\text{ K}$.

Figure S3 shows the magnetic hysteresis loop of the 3QL Cr-doped $(\text{Bi, Sb})_2\text{Te}_3/5\text{QL} (\text{Bi, Sb})_2\text{Te}_3/3\text{QL Cr-doped} (\text{Bi, Sb})_2\text{Te}_3$ sandwich heterostructure (3-5-3 sample) measured by a superconducting quantum interference device (SQUID) based magnetometer at $T = 1.8\text{ K}$. We did not see any additional steps near the coercive fields, indicating the two magnetic TI layers have the same coercive fields ($\mu_0 H$).

II. Determining the Curie temperature of the TI sandwich heterostructure

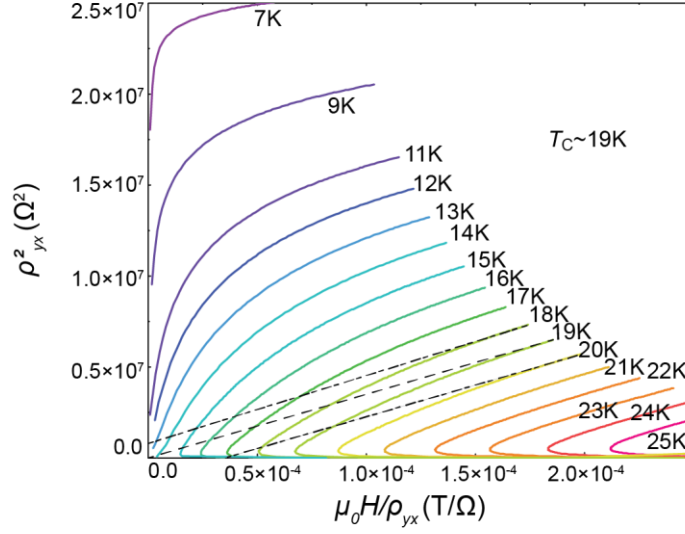


Figure S4 | Arrott plots of the magnetic TI sandwich heterostructure (3-5-3 sample 1). The T_C of this TI sandwich heterostructure is ~ 19 K.

The Curie temperature (T_C) of a ferromagnetic (FM) material can be accurately determined by the Arrott plots. In the limit of high magnetic field ($\mu_0 H$), the Hall resistance ρ_{yx} can be expressed in the form: $\rho_{yx}^2 = a + b\mu_0 H/\rho_{yx}$ (black dotted lines in **Fig. S4**), where a and b are constants¹. When the FM state is approached from above T_C , the slope b of the $\mu_0 H/\rho_{yx}$ term increases and the intercept a changes sign from negative ($T < T_C$, the FM state) to positive ($T > T_C$, the paramagnetic state). **Figure S4** displays the Arrott plots of the 3QL Cr-doped (Bi, Sb)₂Te₃/5QL (Bi, Sb)₂Te₃/3QL Cr-doped (Bi, Sb)₂Te₃ sandwich heterostructure (labeled as 3-5-3 sample 1). The T_C of the 3-5-3 sample 1 is found to be ~ 19 K.

III. Additional transport results of the TI sandwich heterostructure (3-5-3 sample 1)

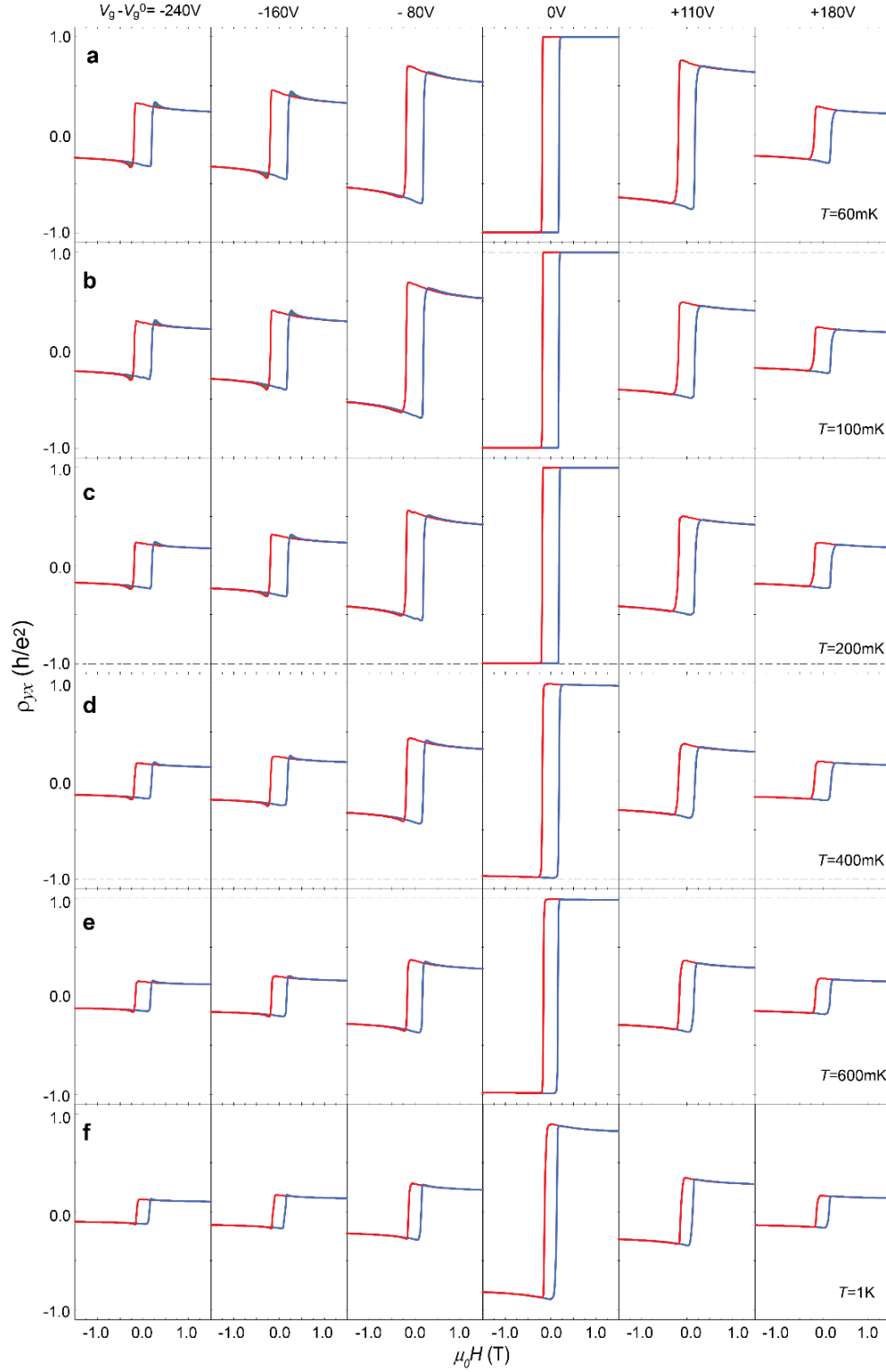


Figure S5 | $\mu_0 H$ dependence of ρ_{yx} of the 3-5-3 sample 1 under different gate voltages ($V_g - V_g^0$) and temperatures. (a) 60mK, (b) 100mK, (c) 200mK, (d) 400mK, (e) 600mK, and (f) 1K.

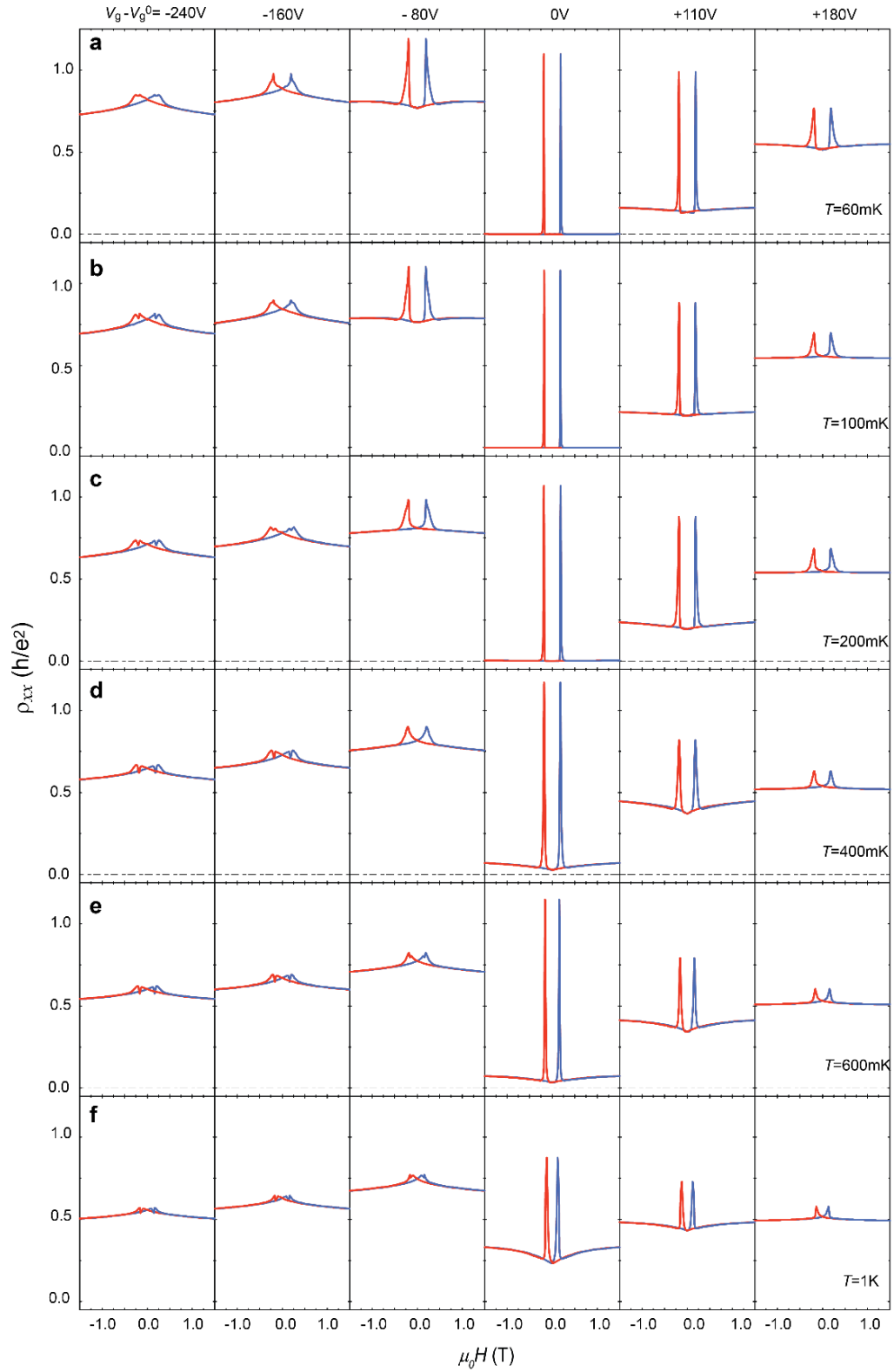


Figure S6 | $\mu_0 H$ dependence of ρ_{xx} of the 3-5-3 sample 1 under different gate voltages ($V_g - V_g^0$) and temperatures. (a) 60mK, (b) 100mK, (c) 200mK, (d) 400mK, (e) 600mK, and (f) 1K.

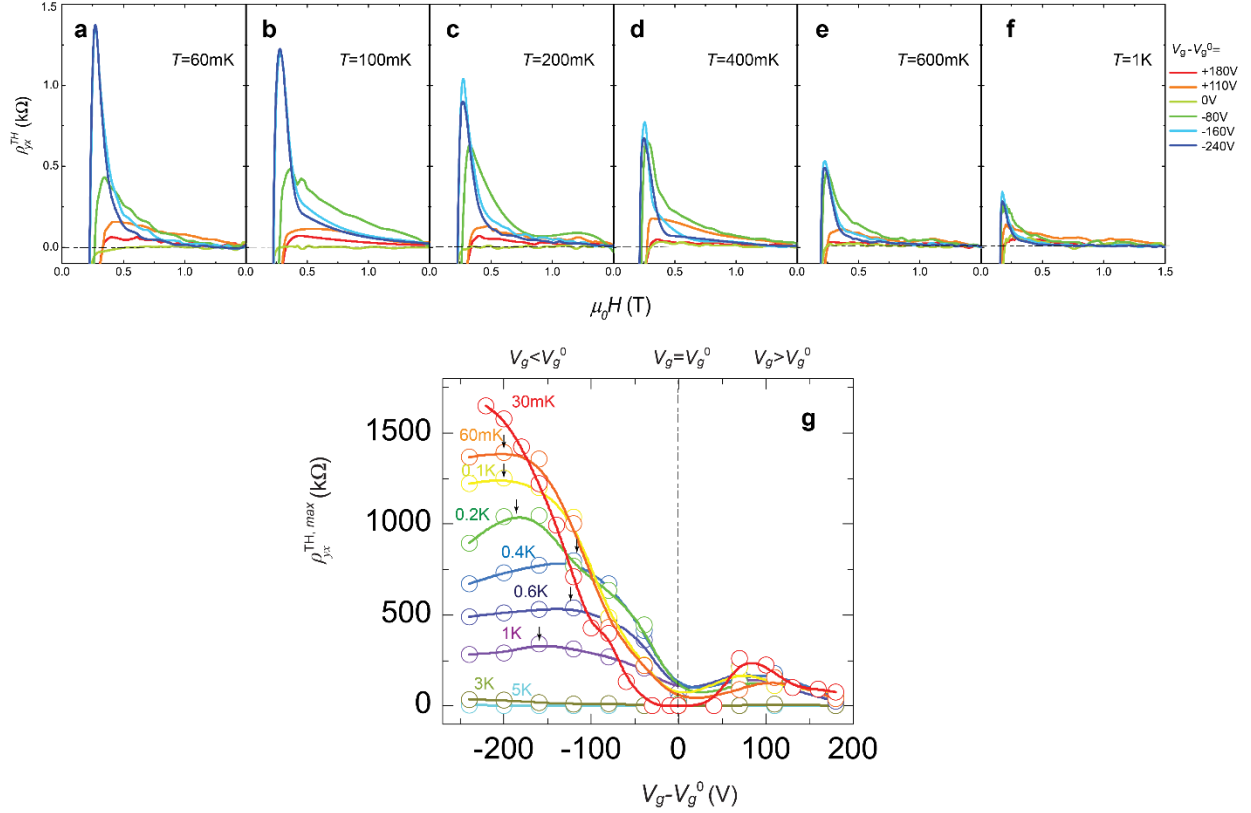


Figure S7 | $(V_g - V_g^0)$ dependence of the TH resistance ρ_{yx}^{TH} of the 3-5-3 sample 1 at different temperatures. (a) 60mK, (b) 100mK, (c) 200mK, (d) 400mK, (e) 600mK, and (f) 1K. (g) The maximum $\rho_{yx}^{\text{TH,max}}$ as a function of $(V_g - V_g^0)$ at different T . $\rho_{yx}^{\text{TH,max}}$ shows a peak denoted by the arrows for $V_g < V_g^0$.

Figures S5 and S6 display the magnetic field $\mu_0 H$ dependence of the Hall resistance ρ_{yx} and the longitudinal resistance ρ_{xx} of the 3-5-3 sample 1. All the data shown in the main text is from this sample. When $V_g = V_g^0$ and $T < 400\text{mK}$, this sample exhibits the perfect quantum anomalous Hall (QAH) state with quantized ρ_{yx} (**Fig. S5**) and vanishing ρ_{xx} (**Fig. S6**). For $V_g < V_g^0$ or $V_g > V_g^0$, with increasing dissipation, ρ_{yx} decreases and ρ_{xx} increases. ρ_{yx} shows a “hump” feature, which has been interpreted as a signature of the topological Hall (TH) effect. This hump feature is more pronounced for $V_g < V_g^0$. We noted that ρ_{xx} shows a twin-peak feature near the coercive field ($\mu_0 H_c$) for $(V_g - V_g^0) = -240\text{V}$ and $T = 60\text{mK}$. This twin-peak feature at $(V_g - V_g^0) = -240\text{V}$ becomes more obvious with increasing T . The V_g at which ρ_{xx} shows this twin-peak feature extends to $(V_g - V_g^0) = -80\text{V}$ at $T = 1\text{K}$. We speculate this phenomenon is likely due to the

weakened magnetic proximity induced FM orders in the middle TI spacer layer. More systematic studies on the dip feature of ρ_{xx} near $\mu_0 H_c$ may be interesting.

The method we used to estimate the TH resistance ρ_{yx}^{TH} at different T and V_g (**Fig. S7a to S7f**) is described in the main text. The ρ_{yx}^{TH} shows a maximum for $V_g < V_g^0$ gradually decreases with increasing T . A summary of $\rho_{yx}^{\text{TH,max}}$ as a function of $(V_g - V_g^0)$ at all temperatures is shown in **Fig. S7g**. The $\rho_{yx}^{\text{TH,max}}$ curve at each T is asymmetric between $V_g < V_g^0$ and $V_g > V_g^0$. When $60 \text{ mK} \leq T \leq 1 \text{ K}$, the ρ_{yx}^{TH} shows a peak as denoted by the arrows when $V_g < V_g^0$. This observation indicates the DM interaction strength is maximized when the chemical potential crosses the bulk valence bands.

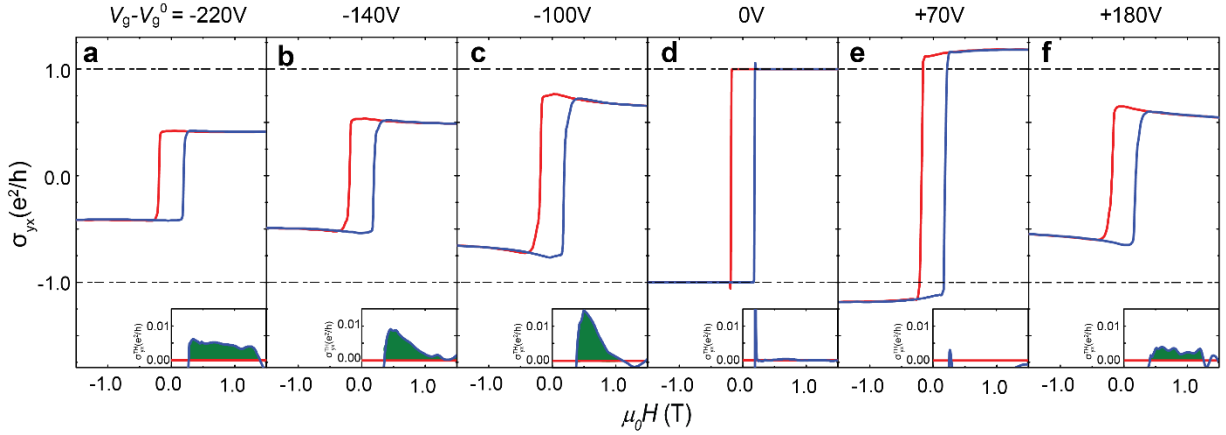


Figure S8 | $\mu_0 H$ dependence of the Hall conductance σ_{xy} at $T = 30 \text{ mK}$ of the 3-5-3 sample 1 under different gate voltages ($V_g - V_g^0$). (a) -220V, (b) -140V, (c) -100V, (d) 0V, (e) +70V, (f) +180V. Insets show the TH conductance σ_{xy}^{TH} deduced from the difference of σ_{xy} measured sweeping $\mu_0 H$ upward (blue) and downward (red).

In order to exclude the possibility that the “hump” feature in ρ_{yx} is an artifact due to the large ρ_{xx} near the $\mu_0 H_c$ regime, we convert ρ_{yx} into the Hall conductance σ_{xy} . We can still see the TH-like “hump” feature in n - and p -type regimes, but V_g for the maximum σ_{xy} is changed. **Figure S8** shows $\mu_0 H$ dependence of σ_{xy} under different V_g s, and the insets show the TH conductance σ_{xy}^{TH} . For $V_g < V_g^0$, σ_{xy}^{TH} displays the “hump” feature. We note that σ_{xy}^{TH} shows a maximum at $(V_g - V_g^0) = -100\text{V}$. This may imply that $(V_g - V_g^0) = -100\text{V}$ corresponds to the chemical potential crossing the bulk valence bands. For $V_g = V_g^0$, σ_{xy}^{TH} is vanishing due to the existence of the perfect QAH effect. At $(V_g - V_g^0) = +180\text{V}$, only a trace of σ_{xy}^{TH} is observed.

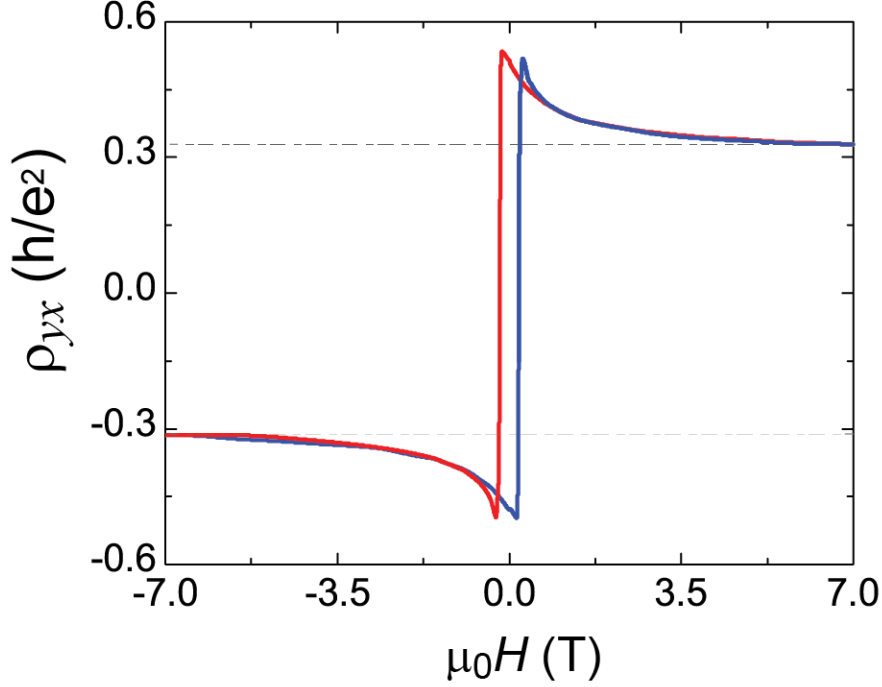


Figure S9 | μ_0H dependence of ρ_{yx} of 3-5-3 sample 1 under $(V_g - V_g^0) = -200V$ at $T=30mK$.

Figure S9 shows the high magnetic field Hall traces of the 3-5-3 sample 1 under $(V_g - V_g^0) = -200V$ at $T=30mK$. At low μ_0H , we can clearly see the TH feature. This observation is consistent with the results shown in **Fig. 2** of the main text. At high μ_0H , the Hall trace shows negative slope and ρ_{yx} saturates when $\mu_0H = 7T$. Next, we will use the following simple argument to explain the “puzzle” why the slope of ρ_{yx} is still negative when hole carriers are introduced.

When the magnetic TI sample is in the QAH state, ρ_{yx} is quantized ($\sim h/e^2$) independent of μ_0H ². According to “standard” understanding of a semiconductor, a zero slope of ρ_{yx} would suggest the carrier density of the QAH sample is infinite. But we know that the carrier density of the QAH sample is actually zero rather than infinite. When the magnetic TI sample deviates slightly from the QAH state, we know that ρ_{yx} is limited to h/e^2 . When electron carriers are introduced, the Hall slope is negative, so ρ_{yx} is unlikely to exceed h/e^2 . When hole carriers are introduced, according to the standard semiconductor theory, the Hall slope should be positive. However, this will make ρ_{yx} exceeds h/e^2 when μ_0H is larger than a critical value. This must not be the case. Therefore, all magnetic TI samples near the QAH regime must show the negative Hall slope.

Here we give a possible reason. We know $\rho_{yx} = \frac{\sigma_{xy}}{\sigma_{xx}^2 + \sigma_{xy}^2}$, if the longitudinal conductance σ_{xx} has a stronger dependence on $\mu_0 H$ near the insulating QAH regime compared to σ_{xy} , $\mu_0 H$ dependence of ρ_{yx} will be primarily determined by the $\mu_0 H$ dependence behavior of σ_{xx} behavior rather than the carrier type of the sample. Since we also observe the TH-like “hump” feature in Hall conductance σ_{xy} (**Fig. S8** and relevant discussion), the hump feature in ρ_{yx} should not be an artifact due to the $\mu_0 H$ dependence of σ_{xx} near the $\mu_0 H_c$ regime.

In addition to the TH effect in the perpendicular $\mu_0 H$, we have also systematically studied the TH effect by rotating the sample with respect to the $\mu_0 H$, as shown in **Fig. S10a**. We found that the chiral spin texture phase in the 3-5-3 sample 1 at $T=2K$ is exceptionally stable under the tilting of the $\mu_0 H$ and the “hump” feature of the TH effect survives as the $\mu_0 H$ is tilted as much as 60° (**Fig. S10b** to **S10i**). This is much higher than the $\theta \sim 10^\circ$ in the EuO film where the destruction of the 2D skyrmion or other chiral spin textures is reported³.

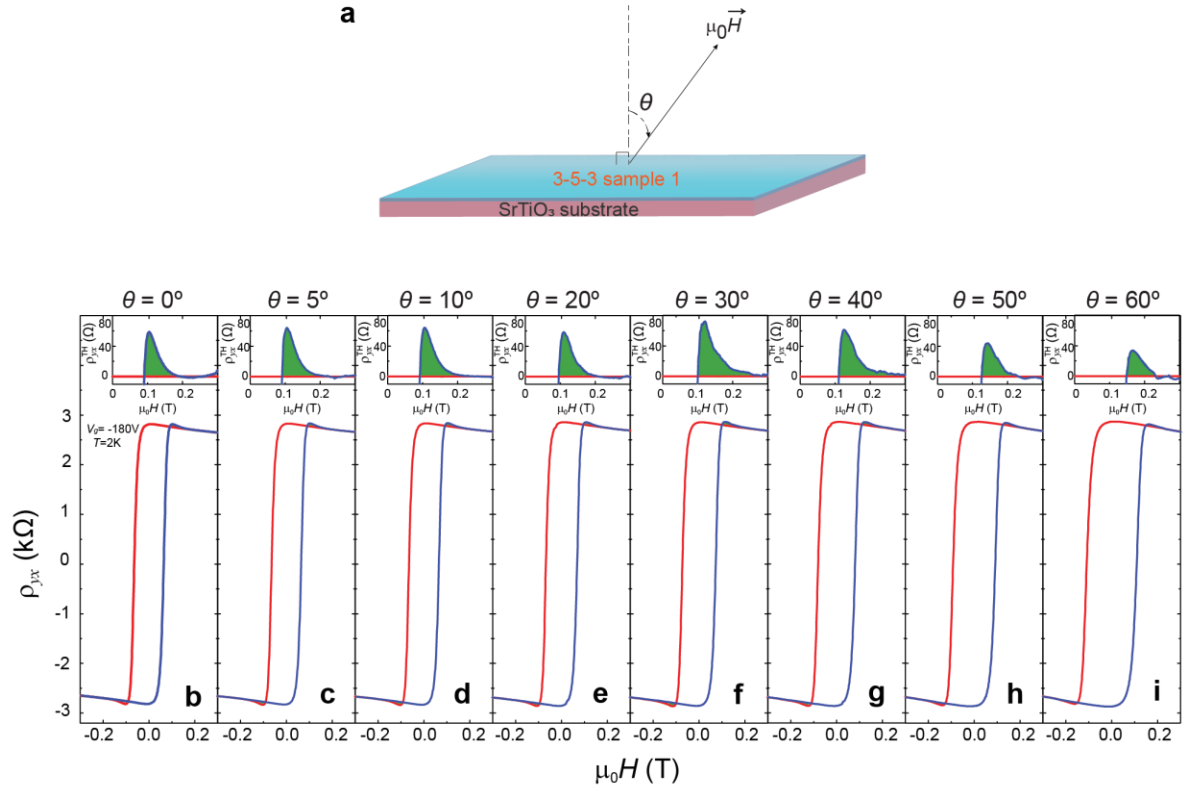


Figure S10 | Tilt angle θ dependence of the TH effect for 3-5-3 sample 1 under $(V_g - V_g^0) = -220\text{V}$ at $T=2\text{K}$. (a) Schematic showing the definition of the tilt angle θ . (b-i) ρ_{yx} of the 3-5-3 sample 1 at the different θ . (b) $\theta = 0^\circ$, (c) $\theta = 5^\circ$, (d) $\theta = 10^\circ$, (e) $\theta = 20^\circ$, (f) $\theta = 30^\circ$, (g) $\theta = 40^\circ$, (h) $\theta = 50^\circ$, (i) $\theta = 60^\circ$. Inset of (b-i): the TH resistance ρ_{yx}^{TH} with the normal Hall resistance ρ_{yx}^{NH} and anomalous Hall resistance ρ_{yx}^{AH} subtracted. The blue (red) curve represents the trace in sweeping $\mu_0 H$ upward (downward).

IV. Transport results of the second 3-5-3 TI sandwich heterostructure (3-5-3 sample 2)

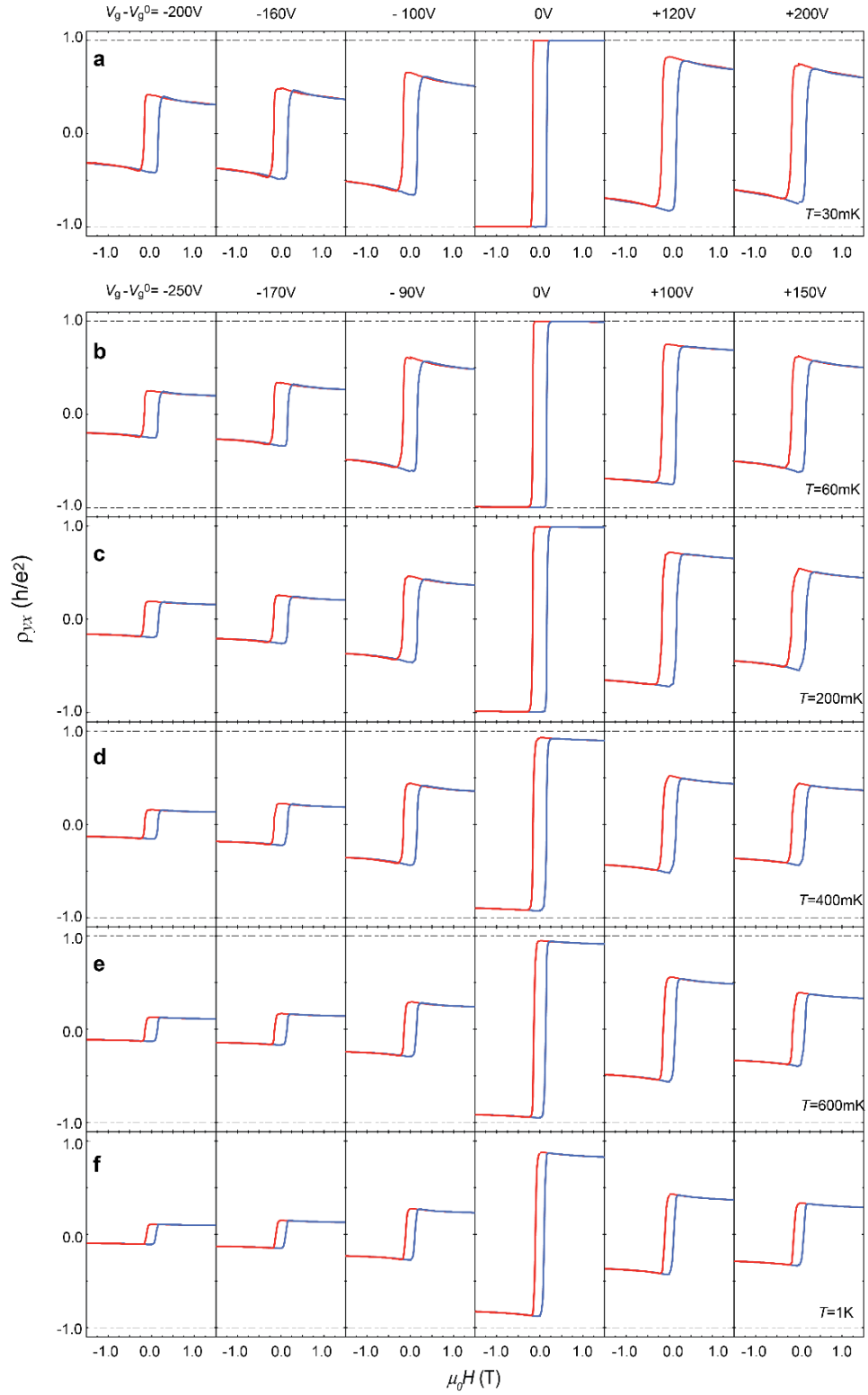


Figure S11 | $\mu_0 H$ dependence of ρ_{yx} of 3-5-3 sample 2 under different gate voltages ($V_g - V_g^0$) and temperatures. (a) 30mK, (b) 60mK, (c) 200mK, (d) 400mK, (e) 600mK, and (f) 1K.

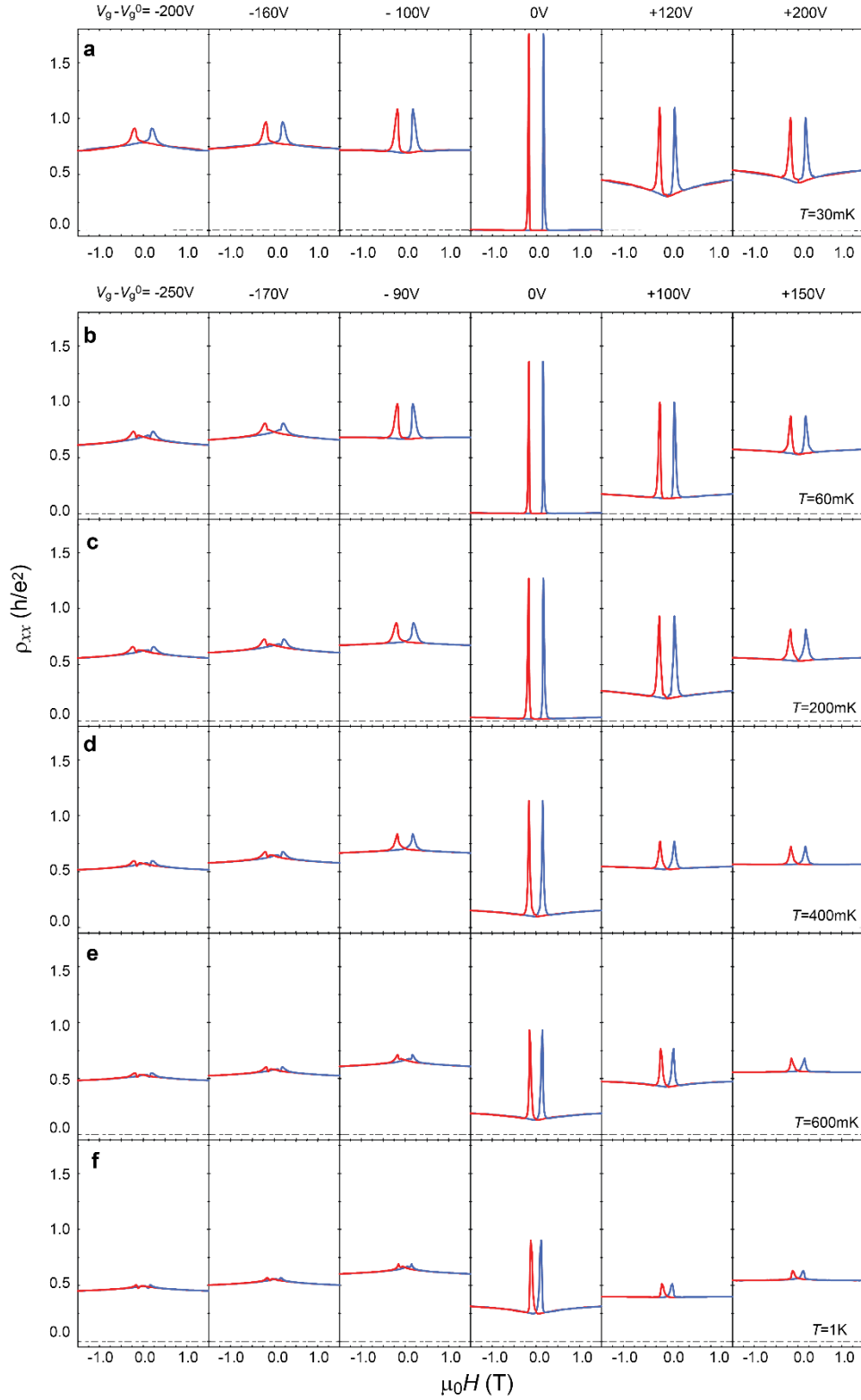


Figure S12 | $\mu_0 H$ dependence of ρ_{xx} of 3-5-3 sample 2 under different gate voltages ($V_g - V_g^0$) and temperatures. (a) 30mK, (b) 60mK, (c) 200mK, (d) 400mK, (e) 600mK, and (f) 1K.

One sample (labeled as 3-5-3 sample 2) with the same configuration as the 3-5-3 sample 1 was also measured to further demonstrate the observation of the concurrence of the QAH and TH effects. **Figures S11** and **S12** show $\mu_0 H$ dependence of ρ_{yx} and ρ_{xx} of the 3-5-3 sample 2 under various gate voltages ($V_g - V_g^0$) and temperatures between 30mK and 1K. The different V_g^0 s for the gate scan at $T=30\text{mK}$ as compared with other temperatures is likely a result of the low temperature charging effect of the SrTiO₃ substrate^{2,4}.

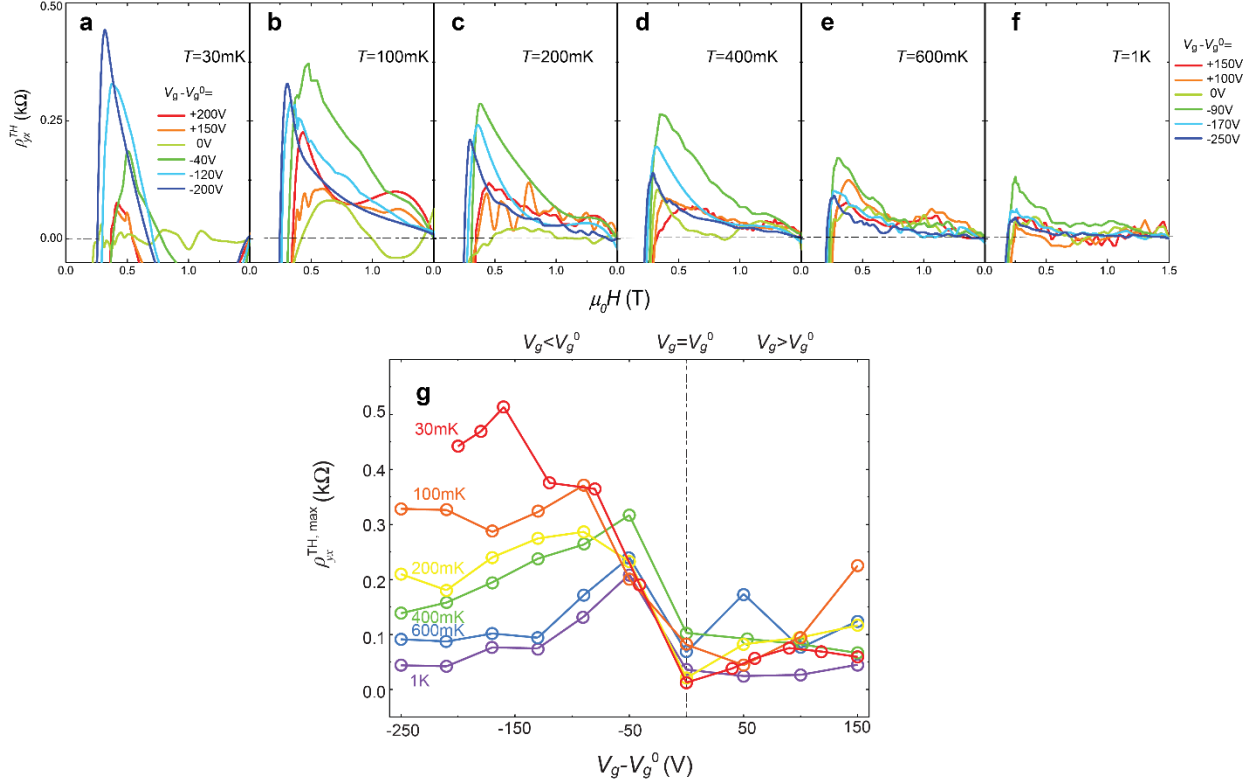


Figure S13 | $(V_g - V_g^0)$ dependence of the TH resistance ρ_{yx}^{TH} of 3-5-3 sample 2 at different temperatures. (a) 30mK, (b) 100mK, (c) 200mK, (d) 400mK, (e) 600mK, and (f) 1K. (g) The maximum $\rho_{yx}^{\text{TH,max}}$ as a function of $(V_g - V_g^0)$ at different T .

Figures S13a-S13f show the $(V_g - V_g^0)$ dependence of the TH resistance ρ_{yx}^{TH} at different temperature. The maximum value of ρ_{yx} (i.e. $\rho_{yx}^{\text{TH,max}}$) at $T=30\text{mK}$ is $\sim 445\Omega$, which is about one-quarter of the value of $\rho_{yx}^{\text{TH,max}}$ found in the 3-5-3 sample 1 (**Figs. 3b, S7a, and S7g**). $\rho_{yx}^{\text{TH,max}}$ becomes smaller with increasing temperatures and is much smaller at $T=1\text{K}$. **Figure S13g** summarizes $\rho_{yx}^{\text{TH,max}}$ as a function of $(V_g - V_g^0)$ at different temperatures. The TH effect of this sample shows similar gate and temperature dependences as the 3-5-3 sample 1 (**Fig. S7g**).

V. Transport results of TI sandwich heterostructures with different sample configurations

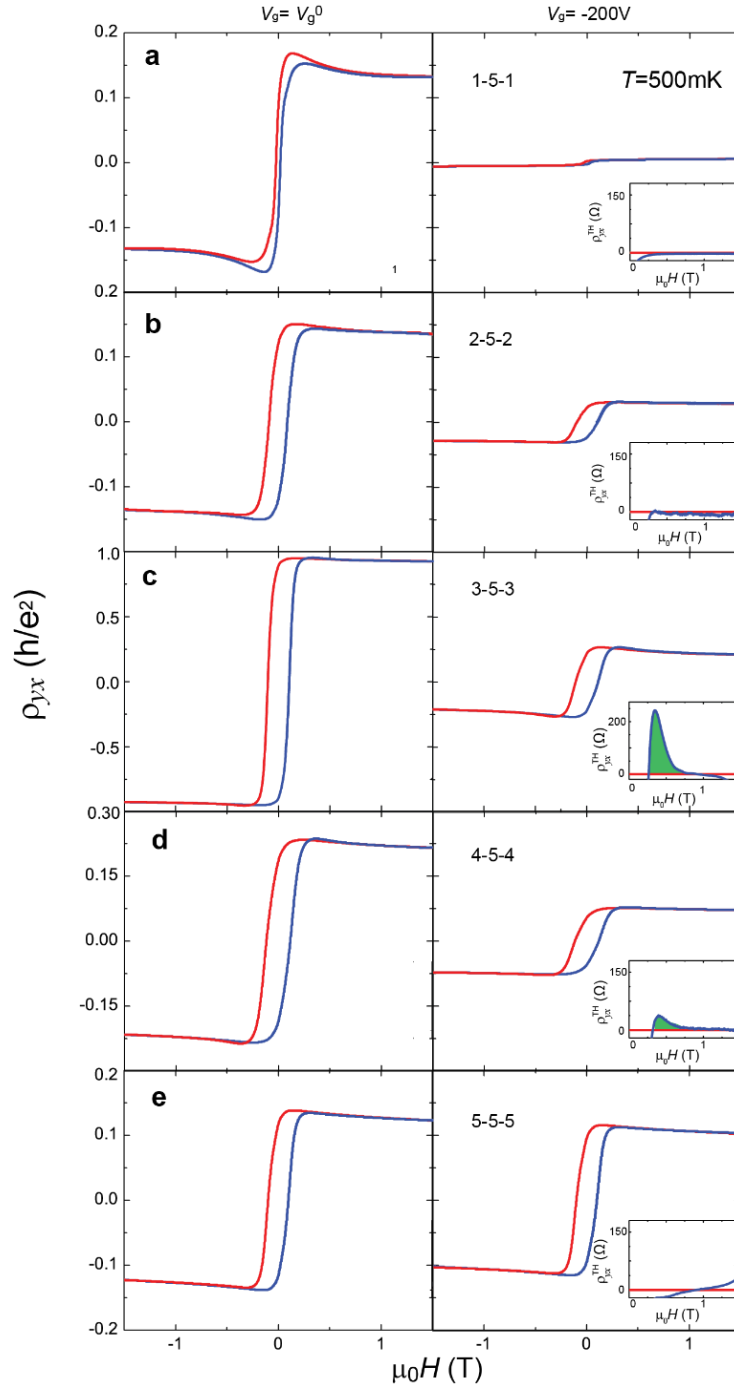


Figure S14 | $\mu_0 H$ dependence of ρ_{yx} of the samples with different configurations measured at $T=500\text{mK}$. (a) 1-5-1, (b) 2-5-2, (c) 3-5-3, (d) 4-5-4, and (e) 5-5-5. The right column is measured at $V_g=V_g^0$, the left one is measured at $V_g = -200\text{V}$. The insets show ρ_{yx}^{TH} at $V_g = -200\text{V}$.

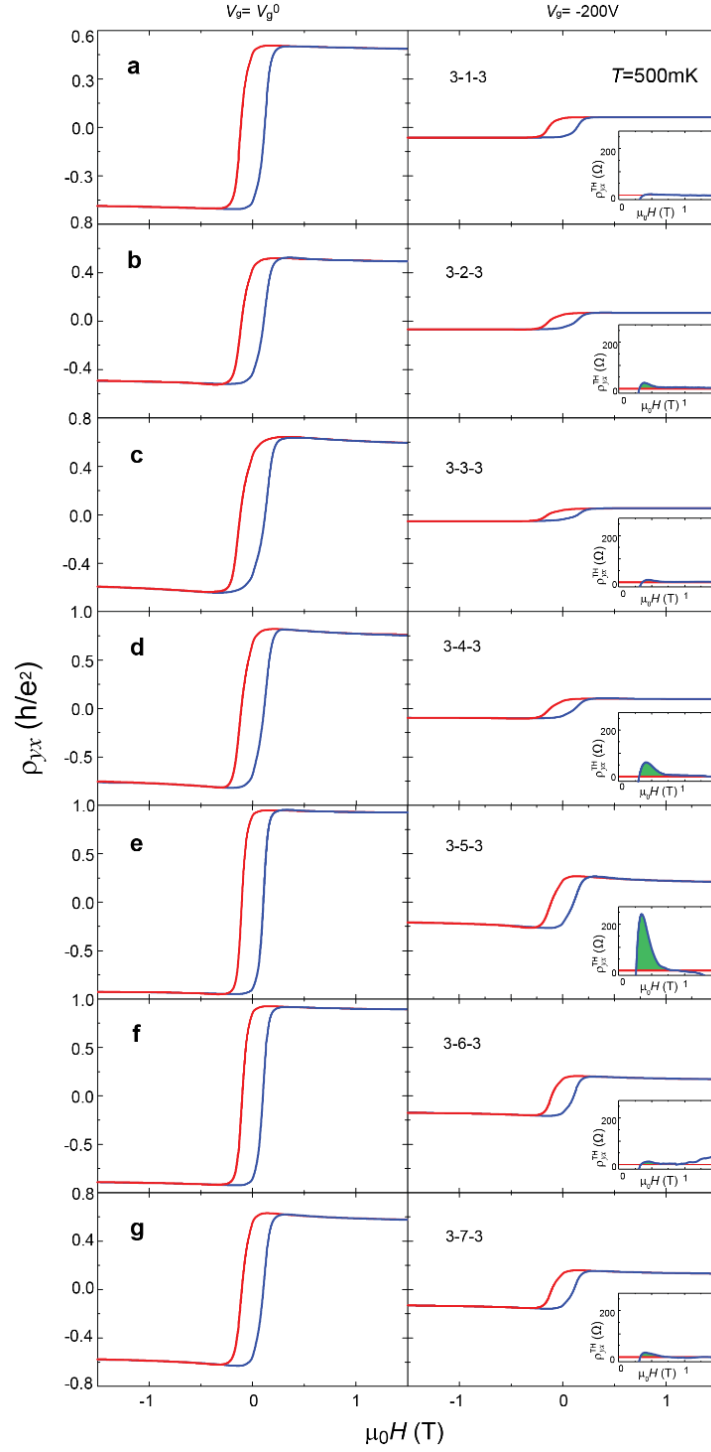


Figure S15 | $\mu_0 H$ dependence of ρ_{yx} of the samples with different configurations measured at 500 mK. (a) 3-1-3, (b) 3-2-3, (c) 3-3-3, (d) 3-4-3, (e) 3-5-3, (f) 3-6-3, and (g) 3-7-3. The right column is measured at $V_g = V_g^0$, the left one is measured at $V_g = -200\text{V}$. The insets show ρ_{yx}^{TH} at $V_g = -200\text{V}$.

As noted in the main text, the asymmetric potential U in the magnetic TI sandwich sample is critical for the formation of the TH effect ⁵. In order to single out the appropriate sandwich heterostructure, in which the TH effect coexists with the QAH effect, we first kept the middle layer of (Bi, Sb)₂Te₃ film to be 5QL and systematically varied the thicknesses of the top and bottom magnetic TI layers (**Fig. S14**). We found the 3 QL magnetic TI layer is optimal for the observation of the concurrence of the QAH and TH effects. Then we kept the top and bottom Cr-doped (Bi, Sb)₂Te₃ film to be 3QL and tuned the thickness of the middle undoped TI layer. We found the 3-5-3 configuration shows the best QAH state at $V_g=V_g^0$ and the TH effect appears when V_g is tuned away from V_g^0 (**Fig. S15**).

Figure S14 shows the $\mu_0 H$ dependence of ρ_{yx} at $V_g=V_g^0$ and $V_g = -200\text{V}$ of the 1-5-1, 2-5-2, 3-5-3, 4-5-4 and 5-5-5 samples. At $V_g=V_g^0$, ρ_{yx} of the 3-5-3 sample is found to be close to the quantized value at $T=500\text{mK}$, while ρ_{yx} of the other four samples is still much less than h/e^2 . Small ρ_{yx} in 1-5-1 and 2-5-2 samples is likely due to the weak magnetization of the thinner magnetic TI layers. This can also be seen from the smaller $\mu_0 H_c$ in these two samples. For the 4-5-4 and 5-5-5 samples, small ρ_{yx} is possibly a result of the thick magnetic TI films inducing dissipative channels in the heterostructures. At $V_g=-200\text{V}$, where the TH effect is shown if applicable. Although both the 3-5-3 and 4-5-4 samples show the ‘‘hump’’ feature of the TH effect, the QAH and TH effects coexist only in the 3-5-3 sample.

In order to optimize the thickness of the middle undoped TI layer, we kept the top and bottom Cr-doped (Bi, Sb)₂Te₃ film to be 3QL and systematically varied the thickness of the middle TI layer. **Figure S15** shows the $\mu_0 H$ dependence of ρ_{yx} at $V_g=V_g^0$ and $V_g = -200\text{V}$ of the 3-1-3, 3-2-3, 3-3-3, 3-4-3, 3-5-3, 3-6-3, and 3-7-3 samples at 500mK. At $V_g=V_g^0$. The ρ_{yx} of 3-5-3 sample is close to the quantized value at $T=500\text{mK}$. At $V_g=-200\text{V}$, the 3-5-3 sample, again, shows the most obvious TH effect. The smaller TH effect in 3-6-3 and 3-7-3 samples are likely because of the existence of too many dissipative channels in the thick heterostructures, which weakens the role of two magnetic TI layers. We note the gating effect is much weaker in the thicker sandwich heterostructures.

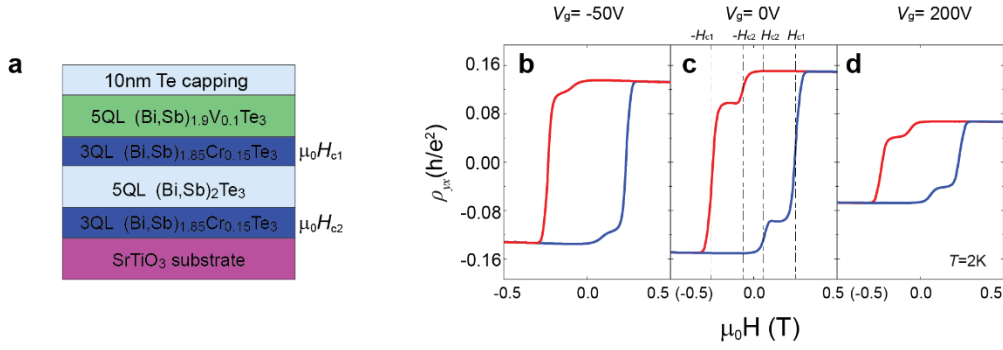


Figure S16 | A control sample to exclude the possibility that the TH “hump” feature is induced by the superposition of two AH components with opposite signs. (a) Schematic of the control sample: 5QL V-(Bi, Sb)₂Te₃ on 3-5-3 sample heterostructure. (b-d) μ_0H dependence of ρ_{yx} under $V_g = -50V$ (b), $0V$ (c), $200V$ (d). Due to the exchange coupling between 5QL V-(Bi, Sb)₂Te₃ and the top 3QL Cr-(Bi, Sb)₂Te₃, the coercive field (μ_0H_{c1}) of the top 3QL Cr-(Bi, Sb)₂Te₃ is enhanced. while the coercive field (μ_0H_{c2}) of the bottom 3QL Cr-(Bi, Sb)₂Te₃ is not affected.

In order to exclude the TH effect observed in the 3-5-3 sample is a result of the superposition of two AH components with opposite signs ⁶, we carried out the following control experiment. We deposited 5QL V-doped (Bi,Sb)₂Te₃ on top of the 3-5-3 sandwich heterostructure (**Fig. S16a**). Since μ_0H_c of V-doped TI is much larger than μ_0H_c of the Cr-doped TI ^{7, 8}, the existence of the exchange coupling effect will increase the μ_0H_c of the top 3QL Cr-doped (Bi,Sb)₂Te₃ layer. This structure configuration favors the formation of the antiferromagnetic alignment between the top and bottom Cr-doped (Bi,Sb)₂Te₃ layers. **Figures S16b to S16d** show μ_0H dependence of ρ_{yx} of the control sample (i.e. the four-layer heterostructure) under $V_g = -50V, 0V, 200V$. μ_0H_{c2} of the bottom 3QL Cr-(Bi, Sb)₂Te₃ is $\sim 0.08T$, while μ_0H_{c1} of the top 3QL Cr-(Bi, Sb)₂Te₃ is $\sim 0.25T$. The “plateau” feature observed for $\mu_0H_{c1} < \mu_0H < \mu_0H_{c2}$ demonstrates the antiparallel magnetization alignment between the two 3QL Cr-(Bi, Sb)₂Te₃ layers ⁸, where the TH “hump” feature disappears rather than being enhanced. This control experiment confirms that the TH effect observed in the 3-5-3 sample is not a result of the superposition of two AH components with opposite signs, as discussed in Ref. ⁶.

VI. Theoretical calculations for the spin susceptibility in magnetic TI

In the main text and the “**Theoretical calculations**” of **Method Section**, we have introduced our model Hamiltonian including both the bulk quantum well (QW) states (H_{QW}) and the topological surface states (SS) (H_{SS}). Both states are coupled to the sample magnetization \mathbf{M} through the Zeeman type of coupling $H_{Zeeman} = -J_H \mathbf{M} \cdot \boldsymbol{\sigma}$. We note that H_{QW} and H_{SS} are actually related to each other by a unitary transformation. Using the unitary transformation $T = (\sigma_z + \sigma_x)/\sqrt{2}$, the H_{SS} can be rotated to the same form as the H_{QW} , as $T^+ H_{SS} T = v_F (k_y \sigma_x - k_x \sigma_y) \tau_x + U \tau_x + m_0 \sigma_z$ and $T^+ H_{Zeeman} T = \mathbf{M}^+ \cdot \boldsymbol{\sigma} + \mathbf{M}^- \cdot \boldsymbol{\sigma} \tau_x$, where $\mathbf{M}^\pm = (\mathbf{M}^t \pm \mathbf{M}^b)/2$. As the overall spin chirality is concerned here, only \mathbf{M}^+ is considered, so the Zeeman coupling on the SS is $H_{Zeeman}^{SS} = -J_H \mathbf{M}^+ \cdot \boldsymbol{\sigma}$, while that on QW states are simply $H_{Zeeman}^{QW} = -J_H \mathbf{M} \cdot \boldsymbol{\sigma}$. We will use the rotated basis for SS in the following calculations.

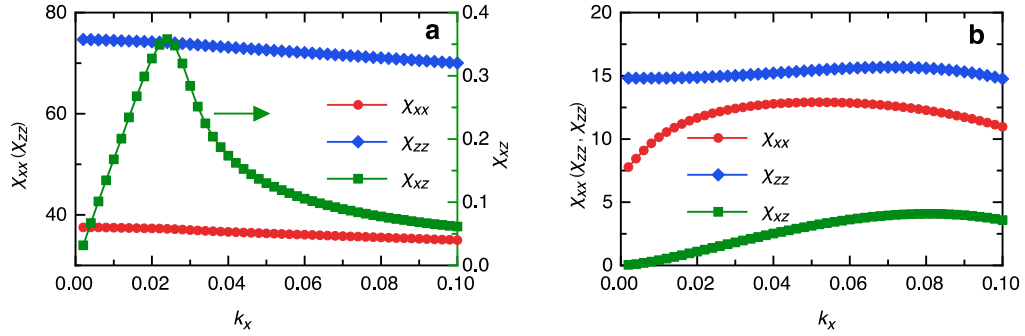


Figure S17 | Comparison between diagonal and off-diagonal susceptibilities. χ_{xx} , χ_{zz} , and χ_{xz} for (a) topological SSs and (b) bulk QW states. The chemical potential μ is at 0.02eV.

Next, we will present a systematic study on the spin susceptibility $\chi_{\alpha\beta}$ ($\alpha, \beta = x, y, z$) through the linear response theory $\chi_{\alpha\beta}(\mathbf{q}) = \frac{T}{2V} \text{Tr}[G_0(\mathbf{q} + \mathbf{k}, i\omega_m) \Gamma_\alpha G_0(\mathbf{k}, i\omega_m) \Gamma_\beta]$, where G_0 is the unperturbed Green’s function, and the spin operator $\boldsymbol{\Gamma}$ is $\boldsymbol{\Gamma} = -J_H \boldsymbol{\sigma}$. Using Matsubara frequency summation, the spin susceptibility $\chi_{\alpha\beta}$ can be given by

$$\chi_{\alpha\beta} = \frac{1}{2} \int d^2k \sum_{m,n} \frac{f_m(\mathbf{k}) - f_n(\mathbf{k} + \mathbf{q})}{i\omega + \varepsilon_m(\mathbf{k}) - \varepsilon_n(\mathbf{k} + \mathbf{q})} \text{Tr}[P_m(\mathbf{k} + \mathbf{q}) \Gamma_\alpha P_n(\mathbf{k}) \Gamma_\beta] \quad (\text{S1})$$

where m, n are band indices, $f = 1/[1 + \exp(\varepsilon - \mu)/k_B T]$ is the Fermi-Dirac distribution, and $P_m(\mathbf{k})$ is the projection operator. ω is chosen to be a small number representing a tiny scattering rate responsible for the potential disorder effect. In our calculations, the temperature is $T=3\text{meV}$

and $\omega = 1\text{meV}$ without loss of generality. Both the diagonal part (e.g. Heisenberg interaction) and off-diagonal part (e.g. DM interaction) of spin susceptibility are studied. We find generally the diagonal part is dominated over the off-diagonal part. In particular, we can see from **Fig. S17** that $\chi_{zz}(\mathbf{q})$ is the largest one, thus suggesting that the system favors out-of-plane ferromagnetism, which is consistent with our experiment. Perpendicular magnetic anisotropy is usually present in such systems with strong spin-orbit coupling^{2,4}.

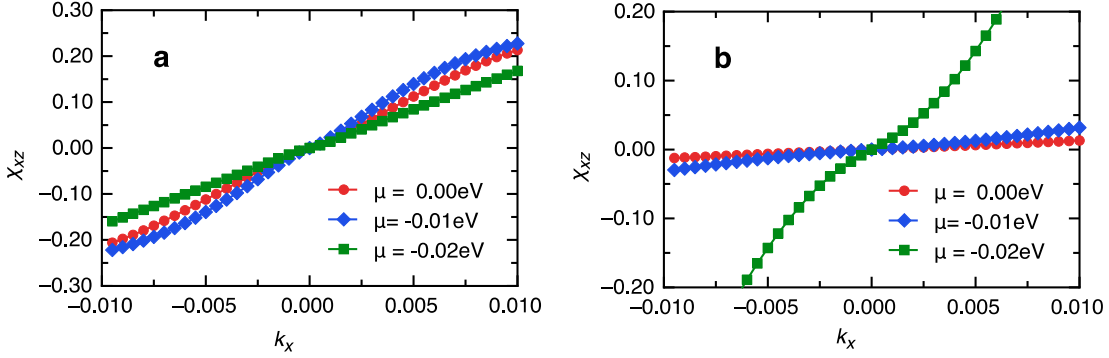


Figure S18 | Linearity between off-diagonal susceptibility and momentum. The susceptibility χ_{xz} as a function of momentum k_x at different chemical potentials for (a) topological SSs and (b) bulk QW states. Linear relations are almost respected at small momenta.

As the spin interaction energy is $E = \sum_{\mathbf{q}} \chi_{ij}(\mathbf{q}) S^i(-\mathbf{q}) S^j(\mathbf{q})$, the off-diagonal part of spin susceptibility responses for the DM interaction and thus is essential for the formation of chiral magnetic domain wall during the magnetic transition. As the system breaks mirror symmetry with respect to xy -plane, $\chi_{xy} = 0$. The electron Hamiltonian H_{QW} or H_{SS} respects mirror symmetry with respect to xz - and yz -planes, the off-diagonal components have the property $\chi_{xz}(q_y = 0) = 0$ and $\chi_{yz}(q_x = 0) = 0$. That means the DM interaction is in the Néel type, consistent with the Moriya rule⁹. Here we focus on χ_{xz} for example, and its momentum dependence is shown in **Fig. S18**. χ_{yz} can directly be related to χ_{xz} through an in-plane rotation due to the full rotation symmetry in the Hamiltonian of the current model. χ_{xz} is clearly an odd function of q_x , and linearly proportional to q_x at small momenta. We choose $q_x = 0.005\text{\AA}^{-1}$ throughout the manuscript. Although nonlinear effects coming from q_x^3 begins to take place at $\mu \leq -0.02\text{eV}$ for QW states, all qualitative results presented are unchanged. Under this momentum choice, the energy dependence of χ_{xz} has been shown in **Fig.4** of the main text for different asymmetric potential U . We have further checked the contribution from intra-band

coupling (i.e. $m = n$ in **Eq. S1**) and inter-band coupling (i.e. $m \neq n$ in **Eq. S1**). We found both contributions are significant, which account for finite susceptibility even when the chemical potential μ locates within the gap (**Fig. S19**).

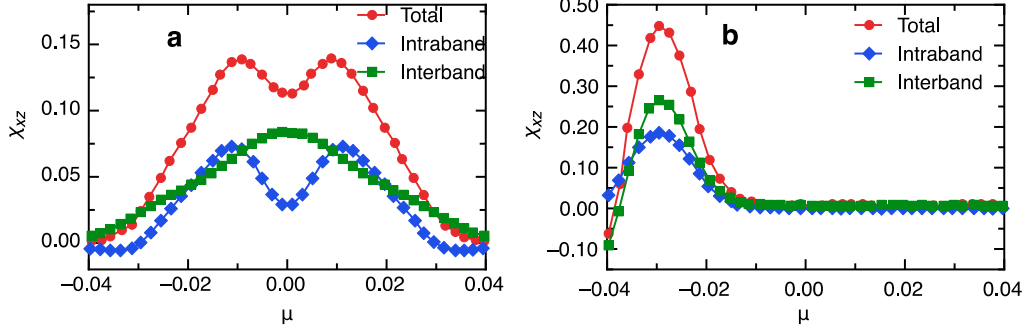


Figure S19 | Separating the intra- and inter-band contributions to χ_{xz} . Both intraband and interband couplings are separated from the total χ_{xz} in cases of (a) topological SSs and (b) bulk QW states.

Since both the asymmetric potential U and the chemical potential μ are changed with tuning the gate voltage V_g in the real experiment, we calculated the spin chirality Q as a function of both U and μ . In the adiabatic regime, the TH resistance ρ^{TH} is proportional to Q , which is quadratic in spin susceptibility χ_{xz} (i.e. $Q \sim \chi_{xz}^2$). Therefore, we plotted χ_{xz}^2 to represent Q as a function of both U and μ in a 3D plot (**Fig. S20a**). The spin chirality Q shows two peaks in the hole doping regime (i.e. $\mu < 0$) when $|U|$ is greater than 0.01eV. At fixed μ , Q is symmetric between positive and negative U and $Q = 0$ at $U = 0$, where the inversion symmetry is preserved. **Fig. S20b** is the 2D color contour plot of **Fig. S20a**. The perfect QAH effect can be realized in the region between two black dashed lines. In order to compare our experimental data (**Fig. 3b** of the main text) with our theoretical calculation, we made a simple approximation that both U and μ are linear in V_g . In other words, the V_g dependence of U and μ in our experiment is a straight line in **Fig. S20b** and the slope of this line characterizes the efficiency of V_g in tuning U and μ .

Figures S20c to S20j show plots of Q vs μ (or Q vs U) along lines 1-8 shown in **Fig. S20b**. Lines 1-4 have larger slopes, suggesting μ is more efficiently tuned than U . The corresponding Q vs μ plots are shown in **Figs. S20c to S20f**. In this case, the strong asymmetric profile of Q with changing V_g comes from the asymmetry between bulk conduction and valence bands, as discussed in our manuscript. When μ is tuned into the magnetization gap the samples show the

perfect QAH effect (light red shadow area). When the slope of the line is reduced, tuning V_g becomes more efficient in changing U and Q decreases monotonically from the hole to electron doping regimes (**Fig. S20f**).

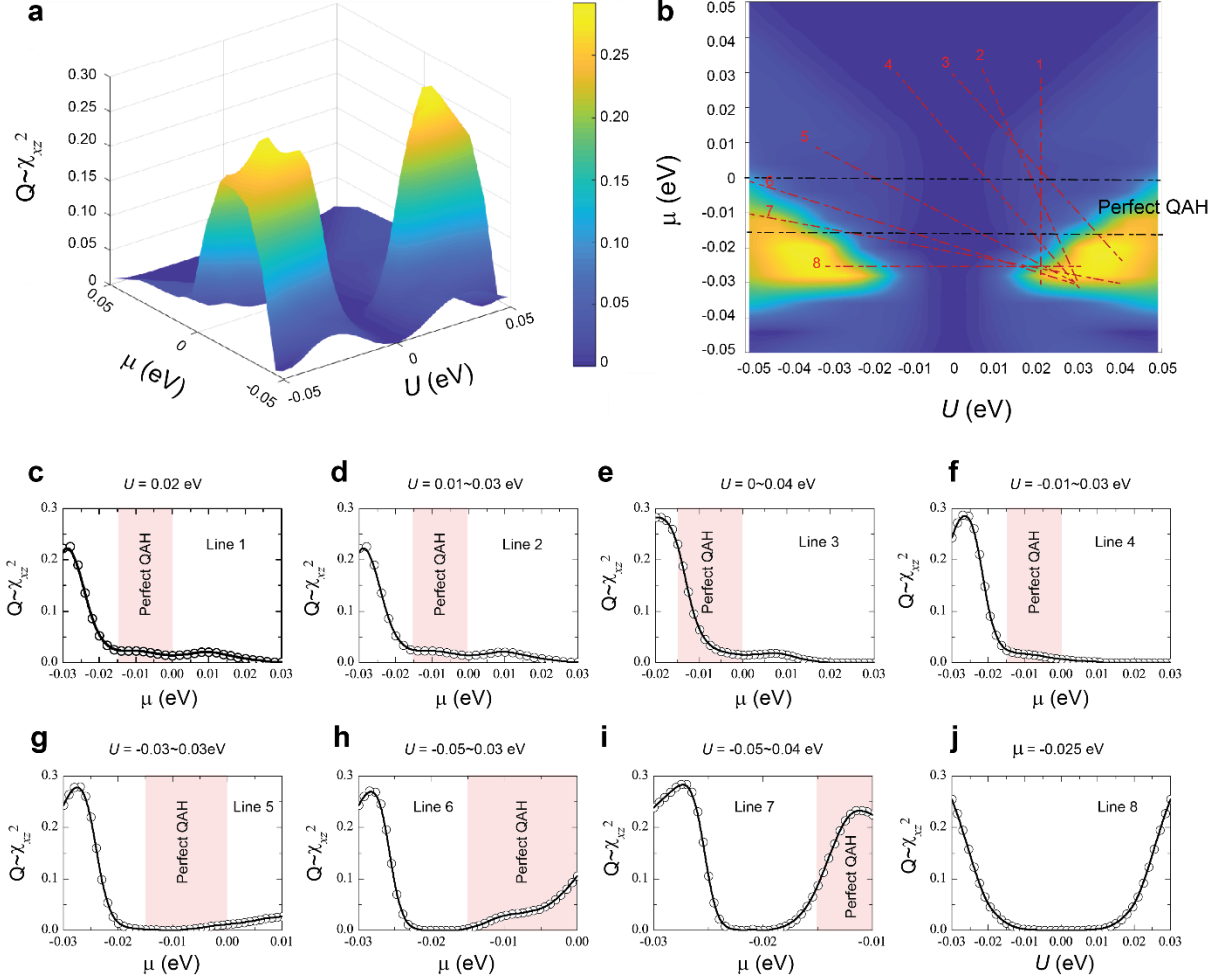


Figure S20 | The calculated spin chirality Q as a function of the chemical potential μ and the asymmetric potential U . (a,b) 3D and 2D contour plots of Q as a function of both U and μ . (c-j) Q vs μ (or Q vs U) plots along lines 1-8 shown in (b). The light red shadow area in (c-i) corresponds to the perfect QAH regime.

For lines 5-8 in **Fig. S20b** with smaller slopes, U is more efficiently tuned instead. As shown in **Figs. S20g** to **S20j**, Q becomes progressively more symmetric as the slope goes towards zero (the zero slope means that the gate voltage only tunes U and μ remains unchanged). As noted above, $Q = 0$ when $U = 0$. This minimum is different from the shallow dip due to the magnetization gap (i.e the perfect QAH regime) in **Fig. S20c** and **S20d**. This minimum moves

away from the perfect QAH regime (light red shadow area) when the slope becomes smaller. Obviously, this is inconsistent with our experimental data. In addition, Q increases monotonically when applying a larger V_g , which is distinctly different from our experiment where the TH effect vanishes under a large positive V_g (**Fig. 3b**). Given the large asymmetric behaviors of TH effect and the vanishing of TH effect at large positive V_g observed in our experiment, we concluded that our system should be in the lines 1-4 region where μ plays the dominant role.

VII. Simulation of the quantum transport through a single chiral magnetic domain wall in magnetic TI

The aim of this section is to explicitly simulate the quantum transport behavior through a single chiral magnetic domain wall in the QAH-TH effect crossover regime with the magnetic TI model by combining the numerical methods of Landauer-Buttiker formalism and iterative Green function methods¹⁰. In particular, we will explicitly demonstrate that in the QAH regime, the TH effect will vanish even in the presence of a chiral magnetic domain wall simply because there are no bulk carriers and the current flows only through the chiral edge channel. We choose the model Hamiltonian H_{QW} described in the “**Theoretical calculations**” of **Method Section**, which can describe both the bulk QW state and the topological SS (with a unitary transformation as shown in **Section VI** above). To simulate the transport behavior, we first perform a tight-binding regularization on this model and obtain the lattice Hamiltonian given by

$$H_{ij} = c_{ij}^\dagger h_{ij} c_{ij} + (c_{i,j+1}^\dagger t_{y+} c_{ij} + c_{i+1,j}^\dagger t_{x+} c_{ij} + h.c.)$$

where

$$\begin{aligned} h_{ij} &= (C_0 + 4C_1/a^2) + (N_0 + 4N_2/a^2)\tau_z + U\tau_x - \mathbf{M}(i,j) \cdot \boldsymbol{\sigma}, \\ t_{y+} &= -C_1/a^2 \sigma_0 \tau_z + iA/2a \sigma_x \tau_x, \\ t_{x+} &= -C_1/a^2 \sigma_0 \tau_z + iA/2a \sigma_y \tau_x \end{aligned}$$

Here we choose the basis $\{+\uparrow, +\downarrow, -\uparrow, -\downarrow\}$. The A term describes spin-orbit coupling, the U term describes the asymmetric potential and \mathbf{M} is the magnetization texture, as a function of spatial coordinates (i, j) .

The form of a single chiral magnetic domain wall is simulated by choosing $\mathbf{M}(i, j) = m_0\{\sin \theta \cos \phi, \sin \theta \sin \phi, \cos \theta\}$, where $\theta = \pi \tanh(\frac{\rho - d_{in}}{d_w})$ labels the magnetization direction forming a chiral magnetic domain wall with chirality $+1$. d_{in} and $d_w \equiv d_{out} - d_{in}$ are the inner radius and the width of the domain, respectively. ρ and ϕ are the polar coordinates of the site at position (i, j) . The whole system in the simulation is chosen to be a square shape with the length L . Four semi-infinite leads with the same ferromagnetic Hamiltonian are attached on the sides of the system for transport measurement. A schematic configuration of the lattice model is shown in **Fig. S21a**.

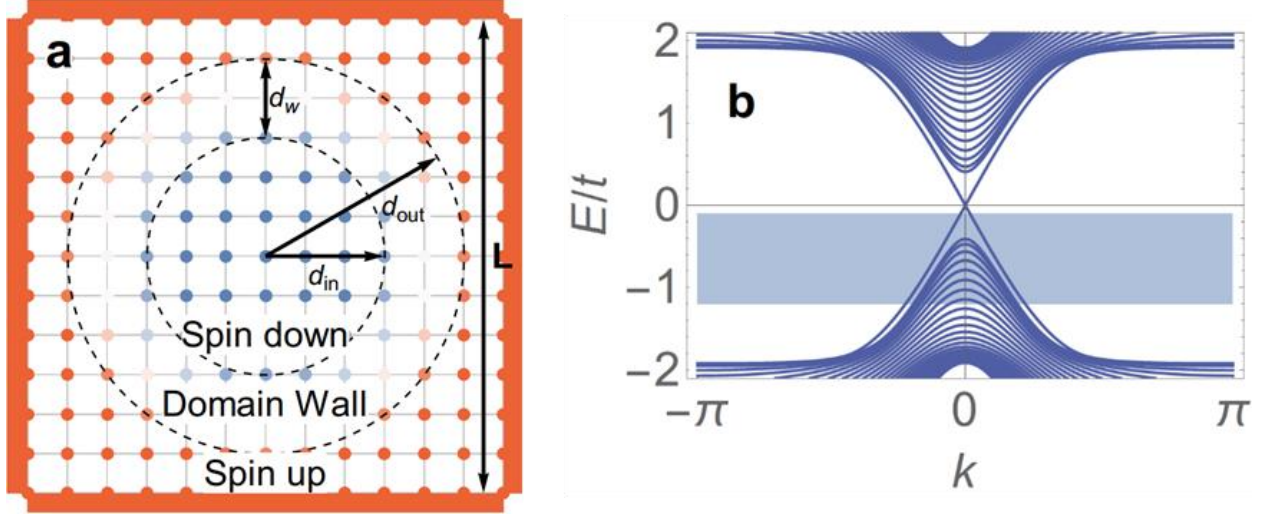


Figure S21 | Schematic configuration of the simulation. (a) The representation of a chiral domain wall in the lattice model. Red and blue sites represent the orientation of magnetization with spin up and spin down, respectively. The outer radius, inner radius, and width of the domain wall are marked with d_{out} , d_{in} and d_w on the graph. The orange stripes represent leads attached to the system. (b) The energy spectrum of a ferromagnetic ribbon with the parameters used in the simulation. The transition region from the hole-doped region to QAH is marked with shade.

Since the purpose of this simulation is to qualitatively demonstrate the transport behavior in the QAH-TH effect crossover regime, we choose the parameters of the tight-binding model as $C_0 = 0, C_1 = N_2 = a = 1, m_0 = 4/3, d_{in} = 6, d_{out} = 32, A_k = 2, U = 0.5, N_0 = -0.8$ and $L = 80$ for the convenience of the numerical simulation. Within this set of parameters, the background is in the QAH state with magnetic moments ferromagnetically aligned. We can further introduce a chiral magnetic domain wall on the ferromagnetic background and extract the TH conductance by comparing the Hall conductance in these two cases. We first show the energy dispersion for a ribbon of background ferromagnetic configuration in **Fig. S21b**, in which chiral edge modes appear inside the bulk band gap. Thus, our system is qualitatively equivalent to the regime that we hope to study in real experimental systems. The blue curve in **Fig. S22a** shows the Hall conductance σ_{yx}^{DW} as a function of the chemical potential tuned from the charge neutral regime to hole-doping regime for the case with a single chiral domain wall. To extract the TH contribution, we also evaluated the Hall conductance in the ferromagnetic case as a background Hall resistance (σ_{yx}^{FM} , red curve in **Fig. S22a**). We define the TH conductance (shown in **Fig. S22b**) as $\sigma_{yx}^{TH} = \sigma_{yx}^{DW} - \sigma_{yx}^{FM}$, similar to that defined in experiments. From **Fig.**

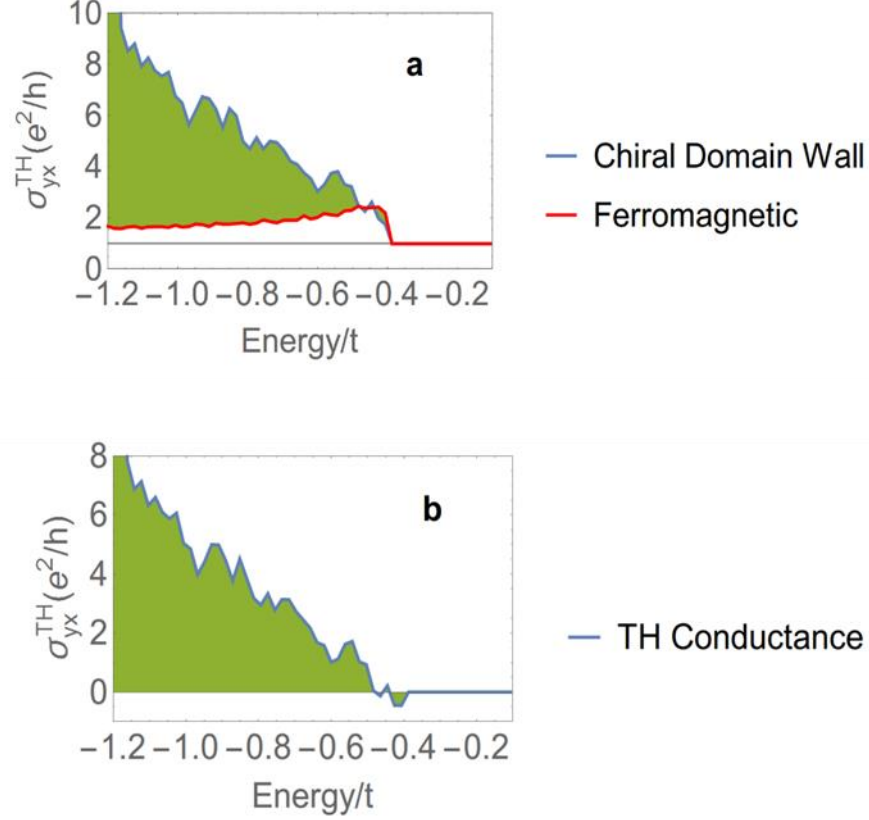


Figure S22 | The extraction of TH conductance. (a) Calculated Hall conductance signals for a Chiral Domain Wall system (blue) and a ferromagnetic system (red) used as background, in the transition region from hole-doped bulk to QAH region. (b) The extracted TH conductance by $\sigma_{yx}^{TH} = \sigma_{yx}^{DW} - \sigma_{yx}^{FM}$. The TH conductance is 0 within the gapped region and increases in the bulk.

S22a, one can see that the Hall conductance σ_{yx}^{DW} keeps quantized when the Fermi energy lies inside the bulk gap for both the ferromagnetic case and chiral domain wall case, thus leading to a zero TH conductance σ_{yx}^{TH} in this regime as shown in **Fig. S22b**. When the Fermi energy is tuned to the hole-doping regime, the Hall conductance σ_{yx}^{DW} increases rapidly when the chiral domain wall is present while the intrinsic anomalous Hall conductance increases first and then saturates to a certain value with decreasing the Fermi energy. As a consequence, we see a rapid increase of TH conductance σ_{yx}^{TH} in the hole-doping regime, as indicated by the shaded region in **Fig. S21b**. Therefore, this simulation qualitatively justifies our claim that the TH effect vanishes in the QAH regime since the transport is due to the chiral edge state which is not affected by the presence of chiral domain walls. It should be pointed out that this simulation here is not for

quantitative comparison and the obtained TH conductance is of magnitudes larger than that observed in experiments for the following two reasons. (i) The simulation here is in the ballistic transport regime without any disorder while the disorder is inevitable in real samples. In our previous work, we have already shown that disorder can significantly reduce the TH conductance due to the reduction of the mean free path¹¹. (ii) Due to the finite size of the lattice in our simulation, we expect that the chirality density induced by the chiral domain walls in our simulation is much larger than that in real experiments. The finite-size effect of the transport also responses for the fluctuation of the Hall conductance seen in the simulation (See **Fig. S22a** and **S22b**).

References

1. Arrott A. Criterion for Ferromagnetism from Observations of Magnetic Isotherms. *Phys. Rev.* **108**, 1394-1396 (1957).
2. Chang C. Z., Zhang J. S., Feng X., Shen J., Zhang Z. C., Guo M. H., Li K., Ou Y. B., Wei P., Wang L. L., Ji Z. Q., Feng Y., Ji S. H., Chen X., Jia J. F., Dai X., Fang Z., Zhang S. C., He K., Wang Y. Y., Lu L., Ma X. C., Xue Q. K. Experimental Observation of the Quantum Anomalous Hall Effect in a Magnetic Topological Insulator. *Science* **340**, 167-170 (2013).
3. Ohuchi Y., Kozuka Y., Uchida M., Ueno K., Tsukazaki A., Kawasaki M. Topological Hall effect in thin films of the Heisenberg ferromagnet EuO. *Phys. Rev. B* **91** (2015).
4. Chang C. Z., Zhang J. S., Liu M. H., Zhang Z. C., Feng X., Li K., Wang L. L., Chen X., Dai X., Fang Z., Qi X. L., Zhang S. C., Wang Y. Y., He K., Ma X. C., Xue Q. K. Thin Films of Magnetically Doped Topological Insulator with Carrier-Independent Long-Range Ferromagnetic Order. *Adv. Mater.* **25**, 1065-1070 (2013).
5. Yasuda K., Wakatsuki R., Morimoto T., Yoshimi R., Tsukazaki A., Takahashi K. S., Ezawa M., Kawasaki M., Nagaosa N., Tokura Y. Geometric Hall Effects in Topological Insulator Heterostructures. *Nat. Phys.* **12**, 555-559 (2016).
6. Groenendijk D. J., Autieri C., Thiel T. C. v., Brzezicki W., Gauquelin N., Barone P., van den Bos K. H. W., van Aert S., Verbeeck J., Filippetti A., Picozzi S., Cuoco M., Caviglia A. D. Berry Phase Engineering at Oxide Interfaces. *arXiv:1810.05619* (2018).
7. Chang C. Z., Zhao W. W., Kim D. Y., Zhang H. J., Assaf B. A., Heiman D., Zhang S. C., Liu C. X., Chan M. H. W., Moodera J. S. High-Precision Realization of Robust Quantum Anomalous Hall State in a Hard Ferromagnetic Topological Insulator. *Nat. Mater.* **14**, 473-477 (2015).
8. Xiao D., Jiang J., Shin J. H., Wang W. B., Wang F., Zhao Y. F., Liu C. X., Wu W. D., Chan M. H. W., Samarth N., Chang C. Z. Realization of the Axion Insulator State in Quantum Anomalous Hall Sandwich Heterostructures. *Phys. Rev. Lett.* **120**, 056801 (2018).
9. Moriya T. Anisotropic Superexchange Interaction and Weak Ferromagnetism. *Phys. Rev.* **120**, 91-98 (1960).
10. Datta S. *Electronic transport in mesoscopic systems*. Cambridge University Press: Cambridge ; New York, 1997.
11. Zhang J.-X., Andreoli D., Zang J., Liu C.-X. Topological Hall Effect in Magnetic Topological Insulator Films. *arXiv:1809.02210* (2018).